Pharmaceutical Sciences and Drug Design
ISSN: 3062-4428
2025, Volume 5, Page No: 360-376

Available online at: www.galaxypub.co/page/journals

Galaxy Publication

Computationally Guided Optimization of a Tetrahydroquinoline Scaffold for Targeting GPER in Cancer Cells

Daniel R. Wilson[1], Laura M. Chen[1]*, Thomas K. Nguyen[1]

[1]Department of Pharmaceutical Sciences, School of Pharmacy, University of California San Diego, San Diego, United States.

***E-mail** ✉ laura.chen@gmail.com

Received: 16 August 2025; **Revised:** 21 November 2025; **Accepted:** 25 November 2025

ABSTRACT

Computational and informatics-driven methodologies have become essential components of modern drug discovery, particularly for the development of targeted anticancer agents with improved selectivity and minimized adverse effects. In the present study, three previously unreported compounds were conceived through a structure-based design strategy and subsequently synthesized. In silico screening predicted favorable pharmacokinetic and toxicity-related properties, as well as strong binding affinity toward the G protein-coupled estrogen receptor (GPER). These computational findings were supported by experimental antiproliferative evaluations conducted in multiple cancer cell lines. To elucidate the molecular basis of receptor–ligand recognition, molecular docking was integrated with molecular dynamics simulations and molecular mechanics/generalized Born surface area (MMGBSA) calculations. The resulting models indicated stable ligand accommodation within the GPER binding cavity, mediated by critical interactions with a cluster of aromatic residues comprising F206, F208 and F278, which are known to govern ligand recognition at this receptor. Biological assessment using the 3-(4,5-dimethylthiazol-2-yl)-2,5-diphenyltetrazolium bromide assay demonstrated that compounds 4, 5 and 7 significantly reduced the viability of MIA Paca-2, RCC4-VA and Hep G2 cancer cells at micromolar concentrations. Collectively, these findings suggest that strategic modification of the GPER pharmacophore can yield novel ligands capable of effectively engaging the receptor and exerting growth-suppressive effects in nontraditional GPER-expressing cancer models.

Keywords: GPER, Tetrahydroquinoline scaffold, Suzuki–Miyaura cross-coupling, Docking, Molecular dynamics simulations, Antiproliferative

How to Cite This Article: Wilson DR, Chen LM, Nguyen TK. Computationally Guided Optimization of a Tetrahydroquinoline Scaffold for Targeting GPER in Cancer Cells. Pharm Sci Drug Des. 2025;5:360-76. https://doi.org/10.51847/qlTwWfAme8

Introduction

Steroid hormones are well recognized as key contributors to tumor initiation and progression [1]. Within this hormone family, estrogen regulates a broad spectrum of physiological and pathological processes through transcription-dependent pathways, commonly referred to as genomic signaling mechanisms [2]. In parallel, estrogen is also capable of eliciting rapid cellular responses via nongenomic signaling, which involves intracellular cascades triggered by membrane-associated receptors, particularly G protein-coupled receptors (GPCRs) [3]. More recently, an estrogen-responsive membrane receptor has been identified as a relevant pharmacological target in breast cancer, stimulating the development of novel ligands for anticancer therapy [3, 4]. This receptor, initially termed GPR30, has since been renamed the G protein-coupled estrogen receptor (GPER) by the International Union of Basic and Clinical Pharmacology (IUPHAR; www.iuphar.org/).

GPER is a member of the seven-transmembrane GPCR superfamily, which represents the largest and most therapeutically relevant class of drug targets in modern pharmacology [5, 6]. It belongs specifically to the class A rhodopsin-like GPCRs and primarily signals through coupling with Gαi/o proteins, while secondary signaling

occurs via Gαs proteins. Activation of GPER initiates a complex network of intracellular signaling pathways, including epidermal growth factor receptor (EGFR) transactivation, mitogen-activated protein kinase (MAPK) signaling, elevation of intracellular cyclic AMP (cAMP) levels, and calcium mobilization [7-9]. The dihydroquinoline derivative G1 was identified as the first synthetic GPER agonist that does not interact with classical estrogen receptors (ERα and ERβ) [10]. This compound shares a common structural scaffold with known GPER antagonists such as G15 and G36, differing primarily in their substituent patterns, which are believed to determine their agonistic or antagonistic behavior [10–13].

GPER has emerged as a promising therapeutic target across multiple cancer types, with reported growth-inhibitory effects observed in renal [14], hepatic [15], and pancreatic [16] cancer models. Notably, GPER-mediated biological responses vary depending on tissue type, disease state, and receptor expression levels [17, 18]. Advances in computational modeling have provided valuable structural insights into the mechanisms underlying GPER activation and inhibition, facilitating the rational discovery of improved ligands [19, 20]. In a prior investigation, docking and molecular dynamics (MD) simulations combined with molecular mechanics/generalized Born surface area (MMGBSA) calculations were employed to elucidate the structural and energetic determinants of ligand recognition at the GPER binding site. That study identified several critical residues involved in ligand binding, including a cluster of aromatic phenylalanines (F206, F208 and F278) and a polar residue, N310, which plays a pivotal role in receptor activation and deactivation processes [21].

Building on these insights, the present work aimed to introduce targeted chemical modifications to the GPER pharmacophore in order to enhance molecular recognition through additional noncovalent interactions and to exploit secondary binding pockets that could improve receptor selectivity and affinity. One modification involved replacing a bromine substituent with a phenyl ring bearing either an electron-withdrawing nitro group at the meta position (compound 4) or an electron-donating methoxy group (compound 5). A second strategy focused on increasing hydrophobic interactions by introducing a tert-butyl substituent on the piperidine ring (compound 7), with the goal of strengthening interactions with the aromatic phenylalanine cluster.

The design process was initiated using a previously synthesized G1 analog developed by our research group, hereafter referred to as G1-PABA [22]. This compound was obtained by modifying the p-aminoacetophenone moiety of G1 with p-aminobenzoic acid, a fragment previously reported to exhibit inhibitory effects in breast cancer cells [22, 23]. Following the synthesis of G1-PABA, compounds 4, 5 and 7 were prepared and evaluated for antiproliferative activity in renal, liver and pancreatic cancer cell lines. All compounds demonstrated half-maximal inhibitory concentration (IC_{50}) values below 50 μM. Furthermore, their binding behavior within the GPER active site was investigated using docking and MD simulations coupled with MMGBSA calculations, enabling a direct comparison between computational predictions and experimental observations.

Materials and Methods

Computational docking and in silico property assessment

To investigate the molecular recognition between GPER and the designed ligands, a computational docking workflow was implemented. Chemical structures of the compounds were initially generated in two dimensions using ChemBioDraw Ultra 12.0 [24]. These representations were subsequently converted into Z-matrix formats using GaussView 5.0 [25], enabling accurate definition of atomic connectivity and hydrogen placement. Structural optimization was carried out using the AM1 semiempirical method as implemented in Gaussian 09, ensuring energetically favorable conformations prior to docking [26].

Docking simulations employed a previously reported and validated three-dimensional model of GPER [20]. All calculations were performed with AutoDock 4.2.6 [27]. Polar hydrogens were incorporated into the receptor structure, and Kollman charges were assigned accordingly, while ligands were parameterized using Gasteiger charges. A focused docking protocol was applied, defining the search space as a cubic grid centered on the Cα atom of residue N310 with dimensions of 60 $Å^3$ and a grid spacing of 0.375 Å. Ligand conformational sampling was conducted using the Lamarckian genetic algorithm, with a population size of 100 individuals and a maximum of 1×10^7 energy evaluations. The resulting docking poses and interaction patterns were analyzed visually using PyMOL v0.99 [28].

Drug-likeness and physicochemical descriptors were calculated using the Molinspiration platform [29], whereas ADME-tox profiles were predicted with DataWarrior software [30].

Construction of membrane-embedded GPER–ligand systems

To mimic a biologically relevant environment, GPER–ligand complexes (GPER-4, GPER-5 and GPER-7) were oriented relative to a phospholipid bilayer using the Orientations of Proteins in Membranes (OPM) server [31]. Fully hydrated POPC bilayers were generated with the CHARMM membrane builder [32], yielding rectangular systems with dimensions of 110.437 × 110.437 × 122.485 Å.

The receptor–ligand complexes were incorporated into the lipid matrix using a replacement-based embedding strategy implemented in CHARMM [33, 34]. Each membrane system consisted of approximately 314 POPC molecules, asymmetrically distributed between the extracellular and intracellular leaflets. Solvation was performed using the TIP3P water model, and physiological ionic strength (0.15 M NaCl) was achieved through system neutralization and ion placement using CHARMM utilities [33].

Molecular dynamics simulations

All-atom MD simulations were carried out using the GPU-accelerated pmemd.cuda engine within AMBER 12 [35]. System topologies were assembled using the LEaP module, applying the ff99SB force field for protein atoms, Lipid11 parameters for membrane lipids, and GAFF for ligand description [36, 37].

Each system underwent a multistep relaxation protocol. Initial energy minimization (10,000 steps) was performed with positional restraints applied to protein and lipid atoms, allowing solvent relaxation. Temperature equilibration was achieved by gradually heating the systems from 0 to 300 K under constant volume (NVT) conditions across two consecutive 1 ns simulations. This was followed by a 1 ns equilibration under constant pressure (NPT) at 300 K and 1 bar with restrained heavy atoms, and an additional 1 ns equilibration with all restraints removed.

Production MD simulations were conducted for 100 ns under periodic boundary conditions in the NPT ensemble. Electrostatic interactions were treated using the particle mesh Ewald (PME) approach [38], while van der Waals forces were truncated at 10 Å. Hydrogen-containing bonds were constrained using the SHAKE algorithm [39]. Temperature regulation employed Langevin dynamics, and pressure was maintained using semi-isotropic coupling to preserve membrane integrity and area per lipid. The integration time step was set to 2 fs, and atomic coordinates were saved every 1 ps for downstream analyses.

Evaluation of molecular dynamics trajectories

The root-mean-square deviation (RMSD) values were determined solely for the backbone Cα atoms, while the radius of gyration (Rg) was assessed for the entire receptor structure, following removal of global translational and rotational movements. Lipid area per headgroup was derived from the formula: area per lipid = (simulation box X dimension × box Y dimension) / total phospholipids per monolayer. Representative structures, reflecting the most thermodynamically favored and biologically relevant states, were extracted via RMSD-based clustering implemented with the GROMOS method in the g_cluster tool, applying a 0.25 nm threshold [40]. These clusters facilitated analysis of key structural traits in the stabilized GPER–ligand assemblies. All figures and molecular renderings were created with PyMOL version 0.99 [28].

Essential dynamics via principal component analysis

To explore correlated atomic fluctuations, principal component analysis (also termed essential dynamics) [41] was conducted using the g_covar and g_anaeig tools from GROMACS version 4.5.3 [42, 43]. A covariance matrix of atomic positional fluctuations was built and diagonalized, producing eigenvectors (describing motion directions) and eigenvalues (indicating motion amplitudes). Trajectories for each GPER–ligand system were then projected onto the principal eigenvectors to delineate the dominant modes of collective motion.

Estimation of absolute binding free energies

Binding free energies for GPER in complex with each ligand were derived via the MM/GBSA approach, employing a single-trajectory strategy [44-51]. Solvent molecules and ions were excluded from trajectories before calculations. For every system, 400 frames were uniformly sampled (at 100 ps intervals) from the equilibrium phase comprising the final 40 ns of each MD run. The overall binding free energy (ΔGbind) was obtained using:

$$\Delta G_{bind} = G^{complex} - G^{receptor} - G^{ligand} \quad (1)$$

$$= \Delta E_{MM} + \Delta G_{GB} + \Delta G_{SA} - T\Delta S \quad (2)$$

Here, ΔEMM denotes the molecular mechanics energy in vacuum (sum of van der Waals ΔEvdw and electrostatic ΔEele components); ΔGGB and ΔGSA represent polar and nonpolar desolvation penalties, respectively; and −TΔS captures the conformational entropy loss upon association. By incorporating the entropic term, the resulting MM/GBSA estimates qualify as absolute binding free energies (ΔGbind).

Determination of entropic terms

The conformational entropy contribution (−TΔS) was quantified for each complex with the MMPBSA.py tool in Amber 12. Owing to the substantial computational resources required for normal-mode calculations, a reduced set of 20 frames per trajectory—spaced every 2 ns across the last 40 ns—was utilized.

Synthetic procedures

Commercially sourced reagent-grade materials were employed directly without additional purification. Reaction monitoring was performed via thin-layer chromatography (TLC) on aluminum-supported silica gel 60 GF254 plates (HX805651) incorporating a UV-active indicator, with detection at 254 nm. Column purification utilized silica gel 60 (230–400 mesh). Uncorrected melting points were recorded on an Electrothermal IA 91000 instrument (Electrothermal, Bibby Scientific, Staffordshire, ST15 OSA, UK). Nuclear magnetic resonance spectra (1H and 13C) were acquired on a Varian Mercury 300 MHz instrument or a Bruker Avance III 750 MHz system, using DMSO-d6 or CDCl3 as solvent and TMS as reference. Chemical shifts (δ) are given in ppm relative to TMS, with J values in Hz. Positive-mode high-resolution electrospray ionization mass spectra (ESI-HRMS) were collected on an Agilent 6545 QTOF LC/MS (Agilent Technologies, Santa Clara, CA, USA).

Preparation of (3aS,4R,9bR)-4-(6-Bromobenzo[d][1,3]dioxol-5-yl)-3a,4,5,9b-tetrahydro-3H cyclopenta[c]quinoline-8-carboxylic acid (G1-PABA, 1)

Both G1-PABA (1) and its tert-butyl-protected analog (compound 7) were prepared according to established protocols previously described by our laboratory [22, 23].

Preparation of (3aS,4R,9bR)-4-(6-(3-Nitrophenyl)benzo[d][1,3]dioxol-5-yl)-3a,4,5,9b-tetrahydro-3H-cyclopenta[c]quinoline-8-carboxylic acid (4)

Compound 4 was synthesized adapting a reported procedure [52]. A mixture of G1-PABA (0.020 g, 0.048 mmol), 3-nitrophenylboronic acid (0.0096 g, 0.057 mmol), PEG2000 (0.060 g, 0.10 mmol), and Pd(OAc)2 (0.004 g, 0.017 mmol) was added to a stirred solution of K2CO3 (0.0266 g, 0.19 mmol) in 1:1 MeOH/H2O (7 mL) **(Scheme 1).** The reaction was heated at 70 °C under nitrogen for 5 h. Upon cooling, the mixture was partitioned with EtOAc (3 × 25 mL). The organics were sequentially washed with water and brine, dried (Na2SO4), and evaporated. Flash chromatography (hexane/EtOAc 7:3) provided compound 4 as a pale brown solid (55% yield); Rf = 0.42 (hexane/EtOAc 7:3); mp 184–185 °C; HPLC purity 97.19%. 1H NMR (750 MHz, CDCl3) δ 8.22 (d, 1H, J = 7.5 Hz, H-4″), 8.14 (bs, 1H, H-2″), 7.68 (d, 1H, J = 7.5 Hz, H-7), 7.67 (s, 1H, H-9), 7.60 (d, 1H, J = 7.5 Hz, H-6″), 7.57 (t, 1H, J = 7.5 Hz, H-5″), 7.26 (s, 1H, H-7′), 7.23 (s, 1H, H-4′), 6.68 (s, 1H, NH), 6.56 (d, 1H, J = 7.5 Hz, H-6), 6.06 and 6.05 (AB, 2H, H-2′), 5.88 (bm, 1H, H-1), 5.69 (bm, 1H, H-2), 4.29 (d, 1H, J = 3.7 Hz, H-4), 4.22 (d, 1H, J = 6.0 Hz, H-9b), 2.67 (m, 1H, H-3a), 1.71 (m, 1H, H-3 down), 1.44 (m, 1H, H-3 up). 13C NMR (187.5 MHz, CDCl3) δ 167.9 (CO2H), 150.4 (C-7a'), 148.3 (C-3′'), 148.2 (C-3′), 146.9 (C-5a), 142.5 (C-1′'), 135.6 (C-6′'), 133.9 (C-2), 133.1 (C-6′), 132.6 (C-9), 132.0 (C-1), 130.6 (C-4′), 129.6 (C-5′'), 129.5 (C-2′'), 124.8 (C-7), 124.4 (C-4′'), 122.6 (C-9a), 119.4 (C-8), 115.3 (C-6), 110.4 (C-4′), 107.1 (C-7′), 101.8 (C-2′), 53.6 (C-4), 45.6 (C-9b), 39.0 (C-3a), 38.9 (C-3). HRMS (ESI) calcd for [C26H20N2O6 + H]+: 457.1400; found: 457.13824.

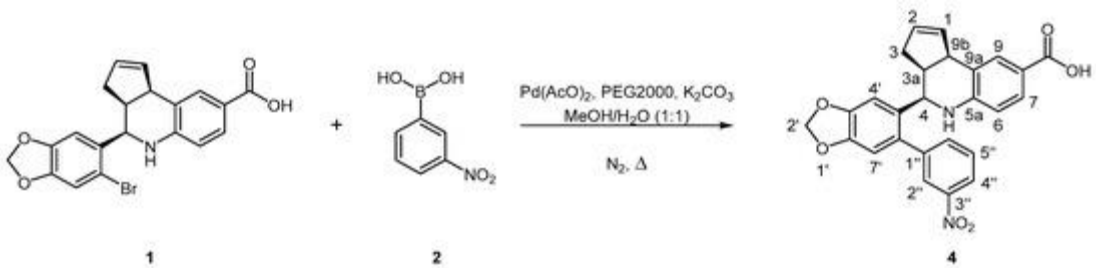

Scheme 1. Assembly of compound 4 through PEG2000-assisted coupling reaction in inert atmosphere.

Assembly of (3aS,4R,9bR)-4-(6-(3-Methoxyphenyl)benzo[d][1,3]dioxol-5-yl)-3a,4,5,9b-tetrahydro-3H-cyclopenta[c]quinoline-8-carboxylic acid (5)

The target molecule 5 was constructed via Suzuki–Miyaura palladium-catalyzed coupling [53]. An aqueous DMF solution containing K2CO3 (0.0266 g, 0.19 mmol) in DMF (1.5 mL) and H2O (1.5 mL) was degassed and stirred under N2 for 15 minutes. G1-PABA (0.020 g, 0.048 mmol), 3-methoxyphenylboronic acid (0.0096 g, 0.057 mmol), PPh3 (0.0015 g, 0.0057 mmol), and Pd(OAc)2 (0.0004 g, 0.017 mmol) were then charged. Heating at 100 °C proceeded for 24 hours **(Scheme 2).** The cooled mixture was diluted and extracted into EtOAc (3 × 25 mL). Organics were washed sequentially with H2O and brine, dried (Na2SO4), and removed in vacuo. Column purification on silica (hexane/EtOAc 8:2) gave 5 as a gray solid (13% yield); Rf = 0.5 (hexane/EtOAc 8:2); mp = 200 °C; HPLC purity 87.31%. 1H NMR (300 MHz, CDCl3) δ 7.69 (d, 1H, J = 7.1 Hz, H-7), 7.68 (s, 1H, H-9), 7.31 (t, 1H, J = 8.8 Hz, H-5″), 7.18 (s, 1H, H-7′), 6.88 (dd, 1H, J = 7.9, 2.9 Hz, H-6″), 6.82 (d, 1H, J = 7.6 Hz, H-4″), 6.78 (d, 1H, J = 1.7 Hz, H-2″), 6.71 (s, 1H, H-4′), 6.54 (d, 1H, J = 8.8 Hz, H-6), 6.02 (m, 2H, H-2′), 5.90 (m, 1H, H-1), 5.69 (m, 1H, H-2), 4.70 (d, 1H, J = 3 Hz, H-4), 3.81 (s, 3H, OMe), 3.81 (dd, 1H, J = 17.6, 8.8 Hz, H-9b), 2.80 (dt, 1H, J = 8.3, 3 Hz, H-3a), 2.64 (dd, J = 15.2, 8.3 Hz, H-3 down), 1.97 (m, 1H, H-3 up). 13C NMR (75 MHz, CDCl3) δ 171.6 (CO2H), 159.3 (C-1″), 150.6 (C-5a), 147.4 (C-3′a), 142.0 (C-7′a), 146.2 (C-1″), 135.1 (C-5′), 132.6 (C-9a), 124.7 (C-6′), 118.8 (C-8), 101.2 (C-2′), 131.8 (C-7), 129.3 (C-9), 128.0 (C-5″), 106.5 (C-7′), 112.3 (C-6″), 121.7 (C-4″), 115.2 (C-2″), 110.3 (C-4′), 114.9 (C-6), 133.7 (C-1), 130.6 (C-2), 53.2 (C-4), 55.2 (OMe), 45.4 (C-9b), 44.5 (C-3a), 31.9 (C-3). HRMS (ESI) calcd for [C27H23NO5 + H]+: 442.1654; found: 442.1646.

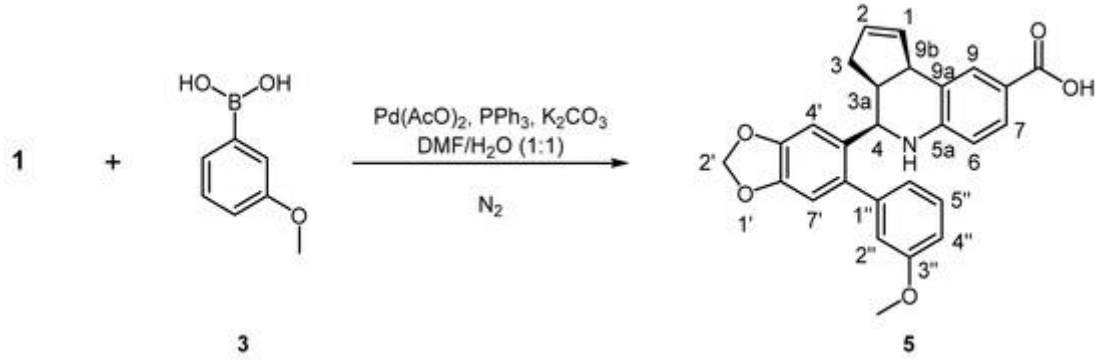

Scheme 2. Construction of compound 5 via Suzuki–Miyaura methodology.

Assembly of (3aS,4R,9bR)-4-(6-Bromobenzo[d][1,3]dioxol-5-yl)-5-(tert-butoxycarbonyl)-3a,4,5,9b-tetrahydro-3H-cyclopenta[c]quinoline-8-carboxylic acid (7)

G1-PABA dissolved in DMF (3.0 mL) was cooled, treated slowly with Et3N (336 μL, 2.413 mmol), and stirred for 30 minutes. Boc2O (0.5268 g, 2.413 mmol) was introduced, the cooling bath removed, and stirring continued overnight at ambient temperature **(Scheme 3).** TLC monitoring guided workup: extraction into EtOAc (3 × 25 mL), washing with H2O and brine, drying (Na2SO4), and solvent removal. Silica gel chromatography (hexane/EtOAc 9:1) afforded 7 as a pale yellow solid (54% yield); Rf = 0.63 (hexane/EtOAc 9:1); mp = 184.3 °C; HPLC purity 95.50%. 1H NMR (300 MHz, CDCl3) δ 7.88 (d, 1H, J = 1.5 Hz, H-9), 7.81 (dd, 1H, J = 8.4, 1.5 Hz, H-7), 7.61 (d, 1H, J = 8.8 Hz, H-6), 6.94 (s, 1H, H-7′), 6.29 (s, 1H, H-4′), 6.17 (m, 1H, H-1), 6.05 (d, 1H, J = 9.7 Hz, H-4), 5.85 (AB, 2H, H-2′), 5.64 (m, 1H, H-2), 3.85 (bd, 1H, J = 8.4 Hz, H-9b), 3.44 (q, 1H, J = 8.3 Hz, H-3a), 2.20 (dd, 1H, J = 16.3, 8.3 Hz, H-3 down), 1.79 (dd, 1H, J = 16.5, 6.8 Hz, H-3 up), 1.40 (s, 9H, OtBu). 13C NMR (75 MHz, CDCl3) δ 165.6 (CO2H), 153.3 (C-carbamate), 147.0 (C-7′a), 146.9 (C-3′a), 141.4 (C-5a), 134.2 (C-9a), 132.2 (C-5′), 114.4 (C-6′), 81.7 (C-tBu), 129.0 (C-9), 127.4 (C-7), 124.7 (C-6), 112.3 (C-7′), 107.9 (C-4′), 133.0 (C-1), 56.0 (C-4), 101.6 (C-2′), 131.8 (C-2), 43.5 (C-9b), 41.6 (C-3a), 34.9 (C-3), 28.2 (3Me-tBu). HRMS (ESI) calcd for [C25H24BrNO6Na] + [M + Na]+: 536.0679; found: 536.0669.

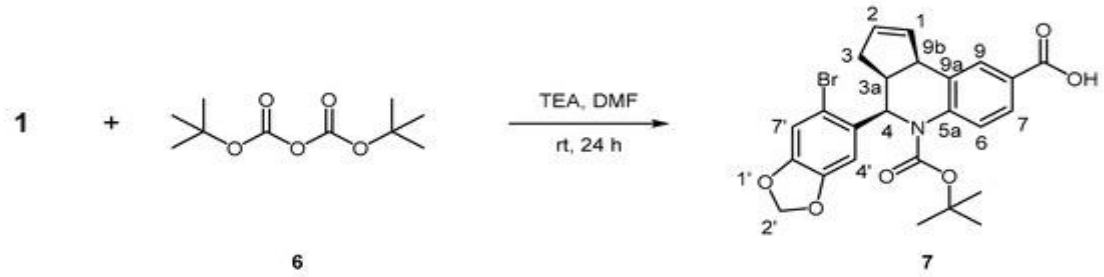

Scheme 3. Installation of Boc protecting group to yield compound 7.

Compound purity assessment via HPLC

Purity evaluations were conducted on an Agilent 1260 Infinity chromatograph (Agilent Technologies, Palo Alto, CA, USA) equipped with quaternary pump (G1311B), automated injector (G1316A), thermostatted column compartment (G1316A), and multi-wavelength UV detector (G1315C). Data acquisition and processing utilized OpenLab CDS EZChrom software. An isocratic mobile phase comprising 40% aqueous 0.2% acetic acid (pH 3.0) and 60% acetonitrile was delivered at 0.5 mL/min through a Zorbax SB-C18 column (5 μm, 4.6 × 150 mm) held at 25 °C. Mobile phases were freshly prepared daily from filtered (0.22 μm) and degassed deionized water. No column reconditioning was necessary between analyses. Compounds exhibiting ≥95% purity were considered suitable.

Maintenance of cell lines

The study involved four human tumor-derived cell lines. RCC4 renal carcinoma cells were engineered to express either empty pcDNA3 vector (neomycin-resistant; RCC4-VA, ECACC N-03112702) or pcDNA3 carrying the VHL gene (RCC4-VHL, ECACC N-0312703), restoring pVHL function associated with altered drug sensitivity. The vector-only line provided a baseline for assessing VHL reinstatement. Pancreatic adenocarcinoma MIA PaCa-2 and hepatocellular carcinoma Hep G2 lines were also included. All media supplements, sera, glutamine, pyruvate, nonessential amino acids, antibiotics, PBS, and insulin were from Life Technologies (Gibco, Invitrogen, CA, USA). MTT and MMS were sourced from Sigma (St. Louis, MO, USA). Automated cultivation and seeding employed the SelecT platform (TAP Biosystems). Hep G2 (ATCC CCL-8065) and MIA PaCa-2 (ATCC CRL-1420) originated from ATCC (Manassas, VA, USA). Hep G2 cultures used Eagle's MEM fortified with 10% FBS, 2 mM glutamine, 1 mM pyruvate, and 100 μM nonessential amino acids. MIA PaCa-2 (bearing K-RAS, P16, and P53 mutations) were propagated in DMEM containing 10% FBS, 2.5% horse serum, 1% glutamine, and 1% penicillin-streptomycin. Both RCC4 variants were sustained in DMEM with 10% FBS, 0.01% 200 mM glutamine, 0.01% antibiotics, and 0.001% G418 (0.5 mg/mL). Incubation conditions were 37 °C, 5% CO2, humidified atmosphere.

Evaluation of cell growth inhibition

Mitochondrial activity was quantified by MTT reduction as a proxy for cell survival [54, 55]. Tumor cells were continuously exposed to compounds for 72 hours. Seeding density was 103 cells per well in 96-well format for all lines. Stock solutions were prepared by diluting pure compounds (3 μL) into medium (597 μL). Robotic dispensing (Biomek FX, Beckman Coulter) delivered 200 μL to triplicate wells across ten concentration points. Positive control: MMS; vehicle control: 0.5% DMSO (kept ≤0.5% to prevent nonspecific effects). Post-incubation (72 h, 37 °C/5% CO2), medium was aspirated and replaced with 100 μL MTT (0.5 mg/mL in phenol red-free MEM). Following 3-hour dye exposure, formazan was solubilized in 100 μL DMSO, and plates were read at 570 nm on a VictorTM reader. Differences relative to vehicle were evaluated by one-way ANOVA, with $p > 0.05$ denoting lack of statistical significance.

Results and Discussion

Docking calculations

Docking analyses were conducted to evaluate the binding affinity and preferred orientations of the designed ligands within the GPER binding pocket. The results indicated that the newly designed compounds were able to access additional receptor cavities beyond those identified in earlier studies [20, 21]. Consistent with previous

findings, GPER molecular recognition was dominated by interactions with key aromatic residues forming a phenylalanine cluster (F206, F208 and F278), along with the polar residue N310. Despite the introduction of substantial chemical modifications to the ligand scaffold—including steric bulk, electronic effects and increased hydrophobicity—both agonist- and antagonist-like ligands displayed binding conformations comparable to those previously reported [20, 21].

Ligand 4, containing a meta-nitro–substituted phenyl group, exhibited close proximity to the phenylalanine cluster, enabling favorable ionic–π interactions between the electron-withdrawing nitro group and the π-electron systems of the aromatic residues. This interaction contributed to a more favorable binding free energy (−8.46 kcal/mol) compared with ligand 5 (−8.36 kcal/mol), which bears an electron-donating methoxy substituent **(Table 1).** In the case of ligand 7, the Boc (di-tert-butyl dicarbonate) group was positioned within 5 Å of residue N310, suggesting a potential role in modulating receptor activation. Additionally, ligand 7 adopted a binding orientation that closely overlapped with that of ligand 5, sharing a similar set of interactions with residues in the binding pocket **(Table 1).**

Table 1. Binding free energies (−ΔG_binding, kcal/mol) and interacting residues of the G protein-coupled estrogen receptor (GPER) with the synthesized ligands as determined by docking analysis.

Ligand ID	Estimated Binding Energy (kcal/mol)	Primary Residues Involved in Nonbonded Interactions
4	−8.46	*F206, H52, L59, L119, N44, Q54, R122***
5	−8.36	*Q53, Q54, H120*, H302*, H307, N310, L59, I279, P303, G58, G306, F278****
7	−8.21	*E51, F278, G58, H120*, H282*, H302*, I279, L59, N310, P303, Q53*, Q54**

* Residue forming H bond.

It should be emphasized that, during the initial docking-based recognition analysis, the key residues—namely the phenylalanine cluster and N310—were not simultaneously engaged in noncovalent interactions with the ligands. Nevertheless, it is well established that GPER possesses multiple binding regions composed of residues with similar chemical characteristics to those found in the orthosteric site [20]. The ligand conformations generated from docking simulations on GPER were subsequently used as starting structures for molecular dynamics simulations, followed by binding free-energy estimations using the MMGBSA methodology. Moreover, all ligands exhibited favorable physicochemical and toxicological–biological profiles, including absorption, distribution, metabolism, excretion and toxicity (ADME-tox), in agreement with Lipinski's rule-of-five criteria for drug-like molecules **(Table 2).** Toxicological–biological screening indicated the absence of adverse effects across all evaluated parameters.

Table 2. Physicochemical and toxicological–biological properties of the ligands evaluated using online prediction platforms. HBD = hydrogen bond donor; MW = molecular weight; Mut = mutagenicity; HBA = hydrogen bond acceptor; Irri = irritability; Ter = teratogenicity; Rep = reproductive effects.

Ligand ID	Molecular Weight (g/mol)	LogP (Lipophilicity)	HBD (Hydrogen Bond Donors)	HBA (Hydrogen Bond Acceptors)	Mutagenicity	Teratogenicity	Irritancy	Reproductive Toxicity
4	456.45	5.62	2	8	None	None	None	None
5	441.48	5.71	2	6	None	None	None	None
7	514.37	5.97	1	7	None	None	None	None

Molecular dynamics simulations

Assessment of equilibration in membrane-embedded GPER–ligand complexes

Initial docking analyses indicated that the investigated compounds formed interaction patterns distinct from those previously reported, largely as a consequence of steric effects [20, 21]. These interactions involved contacts with the aromatic phenylalanine cluster (F206, F208 and F278) as well as the polar residue N310 (data not shown). To verify the persistence of these interactions under dynamic conditions and to gain insight into the conformational behavior of the receptor–ligand complexes, the docked structures were embedded within a membrane environment

and subjected to 100 ns molecular dynamics (MD) simulations. Binding free energies were subsequently estimated using the MMGBSA method, allowing the systems to be evaluated under conditions that more closely resemble the physiological membrane context compared with static docking approaches.

Prior to detailed structural and energetic analyses, the equilibration behavior of the membrane-embedded GPER–ligand systems was carefully examined **(Figure 1).** Three geometric descriptors were monitored to confirm equilibration: the area per lipid of the 1-palmitoyl-2-oleoyl-sn-glycero-3-phosphorylcholine (POPC) bilayer, the root mean square deviation (RMSD) of heavy atoms, and the radius of gyration (Rg) of GPER relative to its initial structure. As shown in **Figure 1a,** the area per lipid initially displayed elevated values during the first 30 ns of simulation but gradually decreased, reaching stable plateaus at approximately 60 ns. At this point, the values converged to 61.03 ± 0.26 Å for GPER-4, 61.34 ± 0.30 Å for GPER-5, and 60.76 ± 0.32 Å for GPER-7.

Analysis of RMSD trajectories revealed that all three GPER–ligand complexes attained structural stability at comparable simulation times, around 50 ns, with average RMSD values of 2.6 ± 0.12 Å, 2.2 ± 0.17 Å, and 2.5 ± 0.11 Å for GPER-4, GPER-5, and GPER-7, respectively **(Figure 1b).** Consistent with these findings, Rg calculations indicated convergence of the systems at approximately 60 ns, yielding values of 26.5 ± 0.1 Å for GPER-4, 26.4 ± 0.13 Å for GPER-5, and 26.5 ± 0.12 Å for GPER-7 **(Figure 1c).** Collectively, these metrics confirmed that all systems reached equilibrium by 60 ns, and subsequent analyses—including root mean square fluctuation (RMSF) calculations—were therefore conducted using the equilibrated portions of the trajectories.

RMSF profiles computed over the final 40 ns of the production simulations demonstrated comparable flexibility patterns across the three complexes **(Figure 1d).** In all cases, the loop region encompassing residues 20–50, which flanks the ligand-binding cavity, exhibited the greatest conformational mobility. Notably, loop 5 (residues 245–251) showed pronounced flexibility exclusively in the GPER-7 system, distinguishing it from the other complexes **(Figure 1d).**

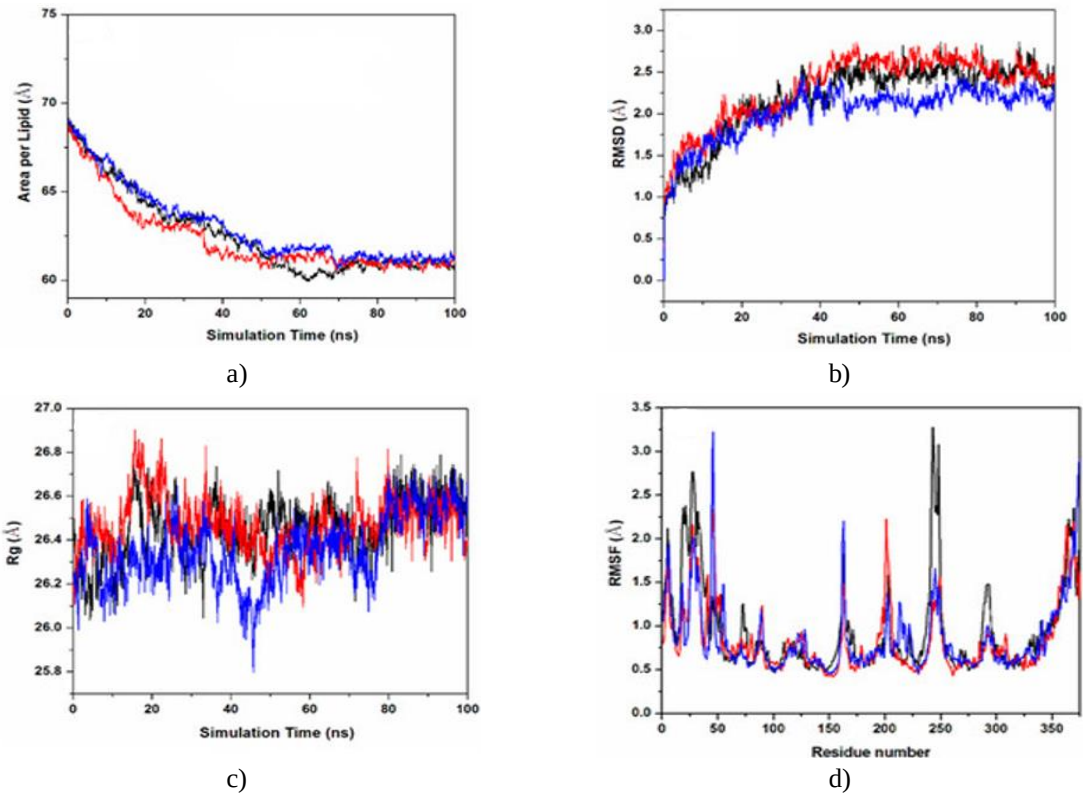

Figure 1. Indicators of dynamic stabilization for membrane-inserted GPER–ligand complexes derived from molecular dynamics (MD) trajectories: (a) temporal evolution of lipid surface area, (b) backbone root mean square deviation (RMSD), (c) receptor compactness expressed as radius of gyration (Rg), and (d) residue-wise root mean square fluctuation (RMSF) for GPER-4 (red), GPER-5 (blue), and GPER-7 (black).

Identification of dominant conformational states

To characterize the structural ensembles sampled by the equilibrated GPER–ligand systems, a clustering procedure was applied to the stabilized segments of the MD trajectories for GPER-4, GPER-5, and GPER-7.

Using a structural similarity threshold of 2.0 Å, distinct differences in conformational diversity were observed among the complexes. The GPER-4 system populated a single conformational state throughout the simulation, whereas GPER-5 and GPER-7 exhibited increased heterogeneity, forming three and five conformational clusters, respectively. The dominant cluster represented the full trajectory for GPER-4, while accounting for 73% and 56% of the sampled conformations for GPER-5 and GPER-7, respectively. The most frequently populated conformers extracted from these clusters were subsequently selected as representative structures for detailed analysis of ligand–receptor interactions.

Essential dynamics analysis

The collective motions underlying the conformational behavior of the GPER–ligand complexes were further explored using Cartesian principal component analysis (cPCA) (see Methods). Decomposition of atomic positional fluctuations resulted in 3375 eigenvectors describing the full motion of the systems; however, only the first 15 modes were sufficient to capture the essential dynamics of the simulations. The contributions of these dominant modes are illustrated in **Figure 2a**, with their respective variance percentages shown in **Figure 2b.** Together, these modes accounted for 69.5% of the total motion in GPER-4, 69.4% in GPER-5, and 75.3% in GPER-7.

Visualization of trajectory projections onto the first two principal components revealed that conformational sampling for all complexes was largely confined within this reduced subspace. Among the three systems, GPER-7 displayed the broadest exploration of the PC1–PC2 plane, indicating enhanced conformational plasticity. In contrast, GPER-4 occupied a more restricted region, while GPER-5 exhibited intermediate behavior with greater extension along PC1 relative to GPER-4. Correspondingly, well-defined and compact conformational basins were most evident for GPER-4, whereas the remaining systems showed less sharply separated states.

A quantitative comparison of overall receptor flexibility was obtained by calculating the trace of the backbone covariance matrix derived from atomic displacement fluctuations **(Figure 2c).** This metric yielded values of 12.71 nm² for GPER-7, 9.94 nm² for GPER-5, and 9.35 nm² for GPER-4, revealing a progressive increase in conformational freedom in the order GPER-7 > GPER-5 > GPER-4. Notably, this hierarchy was consistent with the degree of structural heterogeneity identified in the clustering analysis.

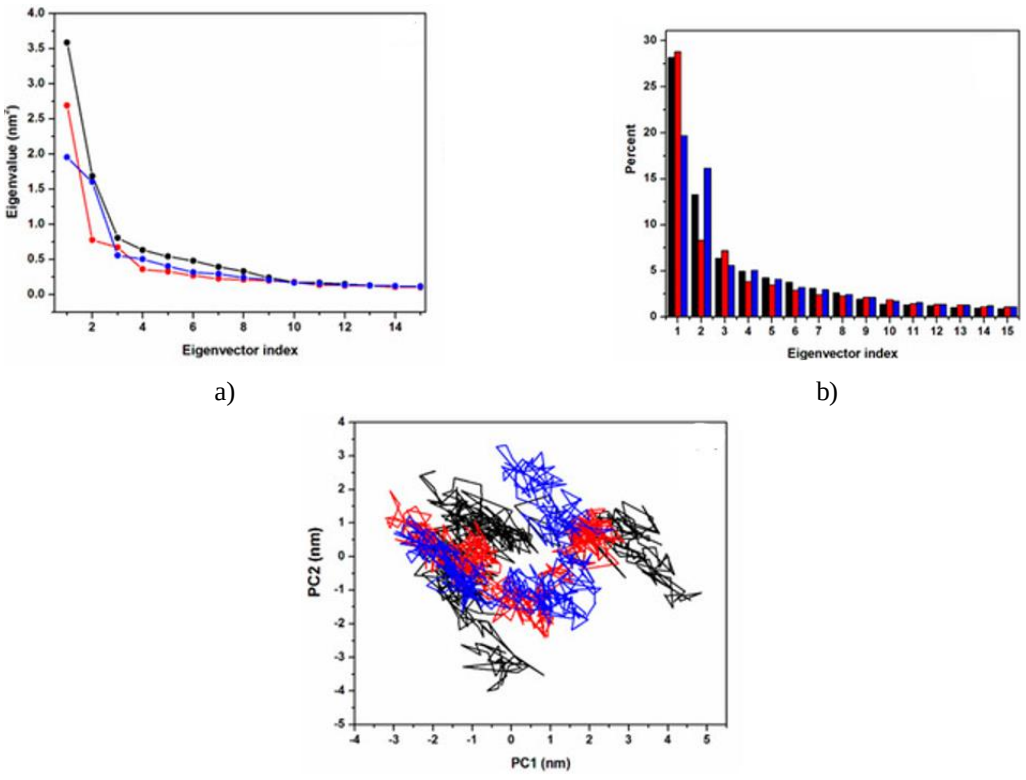

Figure 2. Essential dynamics of the GPER–ligand systems visualized in reduced conformational space. (a) Dominant collective motions extracted from covariance matrix diagonalization for GPER-4 (red), GPER-5

(blue), and GPER-7 (black). (b) Variance contribution associated with each collective mode shown in panel A. (c) Distribution of conformational sampling projected onto the first two principal components (PC1 and PC2) for the three complexes.

Comparison of ligand-induced interaction patterns in GPER

To investigate how ligand binding reshapes the interaction landscape of GPER, structural analyses were performed on representative conformations corresponding to the most frequently populated states identified during clustering **(Figure 3).** Examination of these conformers revealed that each ligand establishes a distinct network of contacts within the receptor binding region, although partial overlap between interaction patterns was observed.

Specifically, compounds 7 and 4 displayed a common interaction footprint involving Gln53, Leu59, Arg122, Met133, and Leu137, indicating that these residues contribute to a shared binding framework for these ligands. In contrast, compound 7 showed a different set of overlapping contacts with compound 5, including Gln53, Leu59, Glu275, Arg122, and Gly58. A third interaction subset was identified for compounds 5 and 4, which both engaged Gln53, Leu59, Leu119, His120, and Arg122.

Despite these pairwise similarities, only three residues—Gln53, Leu59, and Arg122—were found to participate in ligand binding across all complexes. This limited overlap underscores the adaptability of the GPER binding site and demonstrates that modest chemical alterations within the ligand scaffold are sufficient to redirect interaction networks. Consequently, the binding mode of each ligand reflects a balance between conserved anchoring interactions and ligand-specific contacts that arise from pharmacophore modification.

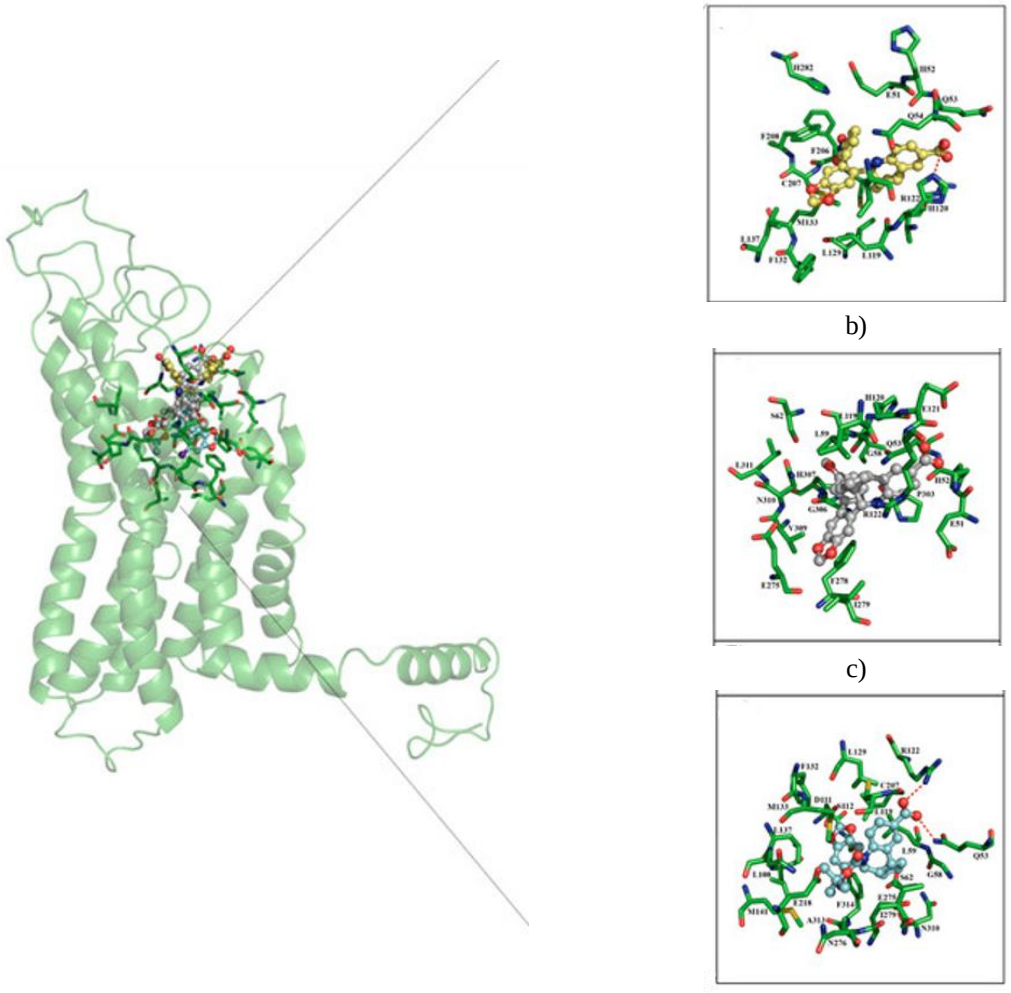

Figure 3. Structural comparison of ligand–GPER interactions. (a) Superposition of all compounds within the GPER binding pocket highlighting regions of close contact. Interaction networks for the most representative

conformations of (b) GPER-4, (c) GPER-5, and (d) GPER-7 are shown. These conformations correspond to the most populated clusters obtained from clustering analysis. Hydrogen-bond interactions are indicated by green dashed lines.

Comprehensive inspection of the representative GPER–ligand complexes indicated that stabilization of all three systems was dominated by hydrophobic contacts within the receptor binding cavity. In particular, residues forming the phenylalanine cluster (F206, F208 and F278) were confirmed as major contributors to ligand stabilization, in agreement with previous reports [20, 21]. Among the investigated compounds, ligand 4 interacted with F206 and F208, whereas ligand 5 established contact with F278; ligand 7 did not engage directly with any residue from this aromatic cluster.

Polar interactions were less prevalent and exhibited ligand-dependent behavior. Only compounds 7 and 4 formed hydrogen bonds or salt bridges through their polar functional groups at the GPER binding site. In the GPER-7 complex, the carboxylate group mediated a hydrogen bond with Gln53 and a salt bridge with Arg122 **(Figure 3b).** In contrast, compound 4 was stabilized by two hydrogen bonds, one involving its carboxyl group and His120 and a second interaction between its nitro substituent and Cys207 **(Figure 3c).** Notably, this latter interaction has previously been associated with stabilization of the receptor in its activated state [20].

The absence of a bromine substituent in the present compounds resulted in the loss of polar interactions analogous to those observed for G1 and G15 with Asn307 or Asn310 [21]. Instead, Asn307 and Asn310 contributed to the stabilization of the GPER-7 and GPER-5 complexes through interactions involving backbone atoms rather than side-chain contacts.

Binding free energy evaluation

To quantify the energetic favorability of ligand binding, absolute binding free energies (ΔG_bind) were calculated for the GPER-4, GPER-5, and GPER-7 complexes using the MMGBSA framework (see Methods). When entropic contributions were included, all three systems exhibited negative ΔG_bind values, indicating thermodynamically favorable complex formation **(Table 3).**

Decomposition of the binding free energy revealed that nonpolar interactions (ΔE_nonpolar = ΔE_vdW + ΔG_npol,sol) constituted the principal stabilizing contribution across all complexes. In contrast, polar energy terms (ΔE_polar = ΔE_ele + ΔG_pol,sol) were energetically unfavorable, opposing the binding process in each case. Entropy calculations further indicated a pronounced reduction in conformational freedom upon ligand association **(Table 3),** suggesting that binding was accompanied by an unfavorable entropic penalty that partially counterbalanced favorable enthalpic contributions.

Among the three systems, GPER-4 displayed the most favorable ΔG_bind value, surpassing those obtained for GPER-7 and GPER-5. This result implies that the nitro-substituted ligand establishes a more energetically optimized interaction network within the GPER binding site compared with the other compounds.

Table 3. Decomposition of binding free energy terms for GPER–ligand complexes (kcal/mol), including polar (ΔE_polar = ΔE_ele + ΔG_ele,sol) and nonpolar (ΔE_nonpolar = ΔE_vdW + ΔG_npol,sol) contributions. Values represent averages ± standard deviation calculated from 400 snapshots extracted every 100 ps from the final 60 ns of MD production trajectories.

System	ΔE_vdw (kcal/mol)	ΔE_ele (kcal/mol)	ΔG_ele,sol (kcal/mol)	ΔG_npol,sol (kcal/mol)	ΔE_polar (kcal/mol)	ΔE_nonpolar (kcal/mol)	ΔG_MM/GBSA (kcal/mol)	TDS (kcal/mol)	ΔG_bind (kcal/mol)
GPER-4	−51.66 (2.9)	15.72 (4.2)	3.50 (0.10)	−6.44 (0.22)	19.22	−58.10	−38.88 (4.0)	−26.43 (1.4)	−12.43
GPER-5	−47.30 (2.78)	19.15 (3.0)	4.70 (0.45)	−6.10 (0.20)	23.85	−53.40	−29.55 (3.2)	−22.34 (2.6)	−7.21
GPER-7	−41.73 (2.5)	−3.90 (0.3)	22.94 (0.3)	−5.52 (0.10)	19.04	−47.25	−28.21 (2.5)	−24.14 (1.3)	−4.07

Antiproliferative activity

GPER has been recognized as a key mediator in oncogenic signaling, with the majority of published studies emphasizing its overexpression and functional relevance in breast cancer. Recent evidence, however, highlights that GPER signaling is highly context-dependent, varying according to tissue-specific expression patterns and the nature of its interacting ligands, which may act either as agonists or antagonists. This ligand- and tissue-selective behavior has broadened the scope for evaluating novel GPER-targeting compounds in cancer models, moving beyond traditional activity assessment strategies [56-58].

In addition to breast malignancies, GPER expression has been reported in several other cancer types, suggesting its potential as a therapeutic target in renal [14], hepatic [15], and pancreatic cancers [16]. Based on this rationale, the antiproliferative potential of the synthesized compounds was examined using a 3-(4,5-dimethylthiazol-2-yl)-2,5-diphenyltetrazolium bromide (MTT) viability assay across a panel of cancer cell lines expressing GPER. The selected models included RCC4-VA and RCC4-VHL renal carcinoma cells, MIA PaCa-2 pancreatic cancer cells, and Hep G2 hepatocellular carcinoma cells.

As summarized in **Table 4**, differential sensitivity to the tested compounds was observed among the evaluated cell lines. Notably, MIA PaCa-2 cells exhibited the greatest susceptibility, with all three compounds producing a clear concentration-dependent reduction in cell viability. Within this model, compound 7 emerged as the most potent antiproliferative agent. This enhanced activity may be associated with the presence of a Boc-protected amine on the piperidine moiety of the GPER pharmacophore **(Figure 4).**

Importantly, the estrogen receptor expression profile of MIA PaCa-2 cells has been well characterized, and therapeutic strategies targeting estrogen receptor signaling are currently employed to inhibit tumor growth in this cancer type [59, 60]. These findings further support the relevance of GPER modulation as a complementary approach in hormone-related cancer treatment.

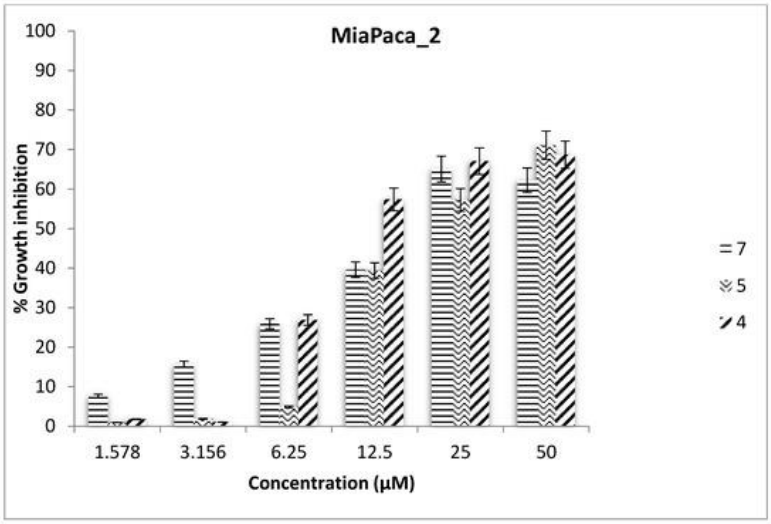

Figure 4. Antiproliferative effects of compounds 4, 5 and 7 in MIA PaCa-2 cells. Data are presented as the mean of three independent experiments; $p < 0.05$.

Table 4. Half-maximal inhibitory concentration (IC_{50}) values determined for the tested ligands across the evaluated cancer cell lines. Values greater than 50 are shown for reference purposes only and are expressed in micromolar (µM).

Ligand ID	IC_{50} RCC4-VA (µM)	IC_{50} RCC4-VHL (µM)	IC_{50} MIA PaCa-2 (µM)	IC_{50} Hep G2 (µM)
7	24.46	>50	14.78	>50
4	>50	>50	18.18	>50
5	39.29	>50	21.15	31.58

The involvement of GPER-mediated signaling was examined in both physiological and pathological contexts, with particular attention to its contribution within the tumor microenvironment of renal, hepatic, and pancreatic cancers—processes that may be modulated by the synthesized compounds. Notably, growth inhibition in RCC4-VA renal carcinoma cells was observed only for compounds 7 and 5, and this effect required higher concentrations than those effective in MIA PaCa-2 cells **(Figure 5).** In RCC4-VA cells, compound 4 displayed a non-monotonic,

non–dose-dependent response, most evident at a concentration of 6.3 µM. This behavior may reflect adaptive cellular mechanisms that counteract drug exposure, such as upregulation of efflux transporters involved in drug extrusion (e.g., P-glycoprotein (PGP) ATPase) or alternative resistance pathways that diminish cellular responsiveness. A similar trend was detected for compound 7 at the highest tested concentration (25 µM), where a slight reduction in efficacy compared with the preceding dose was observed. This type of response corresponds to a biphasic pharmacological profile, a phenomenon previously described in other cancer cell systems (https://www.ncbi.nlm.nih.gov/pmc/articles/PMC4560104/). By contrast, in RCC4-VHL cells, all compounds exhibited antiproliferative activity across the tested concentration range (data not shown). This outcome is particularly noteworthy given the distinct molecular characteristics underlying these renal cancer models, including the deregulation of VHL/HIF signaling pathways and the specific molecular alterations in RCC4-VA cells that contribute to the aggressive tumor phenotype associated with Von Hippel–Lindau syndrome [61, 62]. In Hep G2 hepatocellular carcinoma cells, antiproliferative activity was detected exclusively for compound 5 **(Figure 6),** with effective concentrations comparable to those observed in RCC4-VA cells. This finding may indicate the involvement of a signaling axis linking GPER activation to hypoxia-related pathways, potentially through HIF-1α and vascular endothelial growth factor (VEGF), as previously reported [63]. Moreover, all evaluated cancer models are known to engage molecular mediators associated with hypoxic responses following GPER activation [64, 65]. Collectively, these results reinforce the relevance of GPER as a promising pharmacological target and support the development of novel anticancer therapeutic strategies aimed at modulating its signaling pathway.

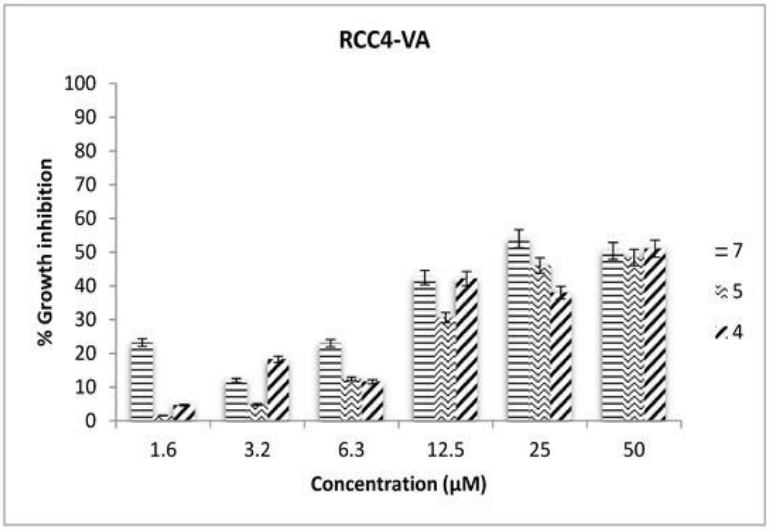

Figure 5. Inhibitory effects of compounds 4, 5 and 7 on RCC4-VA renal carcinoma cells. Values correspond to the mean of three independent experiments ($p < 0.05$).

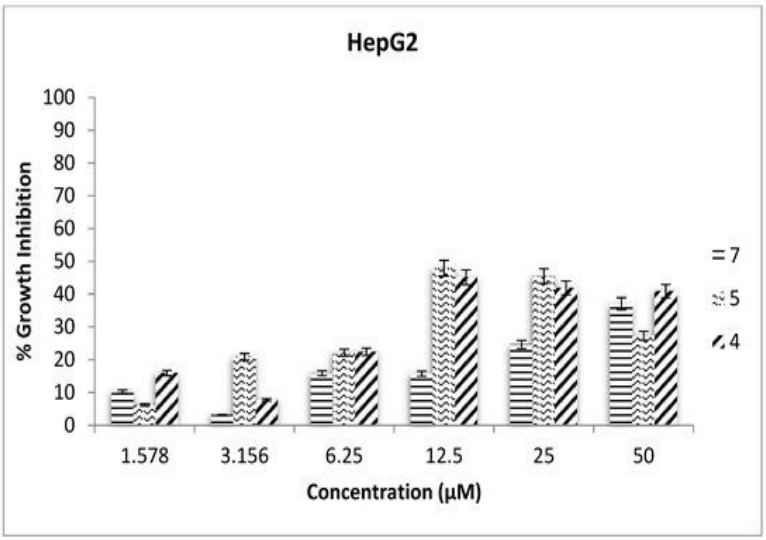

Figure 6. Antiproliferative response of Hep G2 hepatocellular carcinoma cells treated with compounds 4, 5 and 7. Data are presented as mean values from three independent experiments ($p < 0.05$).

Conclusion

Computational strategies, including molecular docking and molecular dynamics simulations, constitute powerful bioinformatic approaches for extracting detailed structural insights that elucidate the molecular determinants governing ligand–receptor recognition. These methodologies therefore represent valuable assets in the rational development of selective therapeutic agents for disease treatment. Within this framework, three novel compounds were designed and demonstrated significant inhibitory effects toward GPER in nonconventional cellular assay systems. Analysis of the chemical modifications introduced into the GPER pharmacophore enabled the identification of critical structural elements—namely, the bromine substituent and the NH moiety of the piperidine ring—as key positions amenable to functionalization for enhancing receptor affinity and biological activity. Importantly, a strong agreement was observed between the experimental in vitro findings and the computational predictions obtained from in silico modeling of GPER–ligand interactions. The data further indicate that GPER exhibits notable binding plasticity, accommodating ligands with planar, aromatic frameworks and tolerating relatively simple chemical alterations that enhance the stereoelectronic features of the pharmacophore. Comparison of the present results with previously reported structural analyses reinforces the conclusion that GPER can interact effectively with chemically diverse scaffolds, particularly those differing by minimal modifications of their core pharmacophoric elements. Despite these encouraging findings, further experimental validation—such as direct binding assays and intracellular Ca^{2+} mobilization studies—will be essential to substantiate the proposed interaction mechanisms. Overall, the strategic application of rational in silico methodologies holds considerable promise for identifying new candidate molecules, thereby expanding the repertoire of potential GPER-targeted agents for cancer therapy.

Acknowledgments: None

Conflict of Interest: None

Financial Support: None

Ethics Statement: None

References

1. llred DC. Issues and updates: Evaluating estrogen receptor-α, progesterone receptor, and HER2 in breast cancer. Mod Pathol. 2010;23(Suppl):S52-9.
2. DeRoo BJ, Korach KS. Estrogen receptors and human disease. J Clin Investig. 2006;116:561-70.

3. Prossnitz ER, Arterburn JB, Sklar LA. GPR30: A G protein-coupled receptor for estrogen. Mol Cell Endocrinol. 2007;265:138-42.
4. Olde B, Leeb-Lundberg LMF. GPR30/GPER1: Searching for a role in estrogen physiology. Trends Endocrinol Metab. 2009;20:409-16.
5. Pierce KL, Premont RT, Lefkowitz RJ. Signalling: Seven-transmembrane receptors. Nat Rev Mol Cell Biol. 2002;3:639-50.
6. Dorsam RT, Gutkind JS. G-protein-coupled receptors and cancer. Nat Rev Cancer. 2007;7:79-94.
7. Revankar CM, Cimino DF, Sklar LA, Arterburn JB, Prossnitz ER. A transmembrane intracellular estrogen receptor mediates rapid cell signaling. Science. 2005;307:1625-30.
8. Thomas P, Pang Y, Filardo EJ, Dong J. Identity of an estrogen membrane receptor coupled to a G protein in human breast cancer cells. Endocrinology. 2005;146:624-32.
9. Filardo EJ, Quinn JA, Bland KI, Frackelton AR. Estrogen-induced activation of Erk-1 and Erk-2 requires the G protein-coupled receptor homolog, GPR30, and occurs via trans-activation of the epidermal growth factor receptor through release of HB-EGF. Mol Endocrinol. 2000;14:1649-60.
10. Bologa CG, Revankar CM, Young SM, Edwards BS, Arterburn JB, Kiselyov AS, et al. Virtual and biomolecular screening converge on a selective agonist for GPR30. Nat Chem Biol. 2006;2:207-12.
11. Burai R, Ramesh C, Shorty M, Curpan R, Bologa CG, Sklar LA, et al. Highly efficient synthesis and characterization of the GPR30-selective agonist G-1 and related tetrahydroquinoline analogs. Org Biomol Chem. 2010;8:2252-9.
12. Dennis MK, Burai R, Ramesh C, Petrie WK, Alcon SN, Nayak TK, et al. In vivo effects of a GPR30 antagonist. Nat Chem Biol. 2009;5:421-7.
13. Dennis MK, Field AS, Burai R, Ramesh C, Petrie WK, Bologa CG, et al. Identification of a GPER/GPR30 antagonist with improved estrogen receptor counterselectivity. J Steroid Biochem Mol Biol. 2011;127:358-66.
14. Guan B-Z, Yan R-L, Huang J-W, Rui-Ling Y, Zhong Y-X, Chen Y, et al. Activation of G protein coupled estrogen receptor (GPER) promotes the migration of renal cell carcinoma via the PI3K/AKT/MMP-9 signals. Cell Adhes Migr. 2018;12:109-17.
15. Chaturantabut S, Shwartz A, Evason KJ, Cox AG, Labella K, Schepers AG, et al. Estrogen activation of G-protein-coupled estrogen receptor 1 regulates phosphoinositide 3-kinase and mTOR signaling to promote liver growth in zebrafish and proliferation of human hepatocytes. Gastroenterology. 2019;156:1788-804.
16. Cortes E, Sarper M, Robinson B, Lachowski D, Chronopoulos A, Thorpe SD, et al. GPER is a mechanoregulator of pancreatic stellate cells and the tumor microenvironment. EMBO Rep. 2019;20:46556.
17. Wang C, Lv X, Jiang C, Davis JS. The putative G-protein coupled estrogen receptor agonist G-1 suppresses proliferation of ovarian and breast cancer cells in a GPER-independent manner. Am J Transl Res. 2012;4:390-402.
18. Wang C, Lv XY, He C, Hua G, Tsai M-Y, Davis JS. The G-protein-coupled estrogen receptor agonist G-1 suppresses proliferation of ovarian cancer cells by blocking tubulin polymerization. Cell Death Dis. 2013;4:1-11.
19. Rosano C, Ponassi M, Santolla MF, Pisano A, Felli L, Vivacqua A, et al. Macromolecular modelling and docking simulations for the discovery of selective GPER ligands. AAPS J. 2015;18:41-6.
20. Méndez-Luna D, Martínez-Archundia M, Maroun RC, Ceballos-Reyes G, Fragoso-Vázquez M, González-Juárez D, et al. Deciphering the GPER/GPR30-agonist and antagonists interactions using molecular modeling studies, molecular dynamics, and docking simulations. J Biomol Struct Dyn. 2015;33:2161-72.
21. Méndez-Luna D, Bello M, Correa-Basurto J. Understanding the molecular basis of agonist/antagonist mechanism of GPER1/GPR30 through structural and energetic analyses. J Steroid Biochem Mol Biol. 2016;158:104-16.
22. Zacarias-Lara OJ, Mendez-Luna D, Martinez-Ruiz G, Garcia-Sanchez JR, Fragoso-Vazquez MJ, Bello M, et al. Synthesis and in vitro evaluation of tetrahydroquinoline derivatives as antiproliferative compounds of breast cancer via targeting the GPER. Anticancer Agents Med Chem. 2019;19:760-71.
23. Martínez-Muñoz A, Prestegui-Martel B, Mendez-Luna D, Fragoso-Vazquez MJ, García-Sánchez JR, Bello M, et al. Selection of a GPER1 ligand via ligand-based virtual screening coupled to molecular dynamics simulations and its anti-proliferative effects on breast cancer cells. Anticancer Agents Med Chem. 2019;18:1629-38.

24. ChemBioDraw Ultra 12.0. 2020. Available from: cambridgesoft.com (accessed 2020 Nov 12).
25. Dennington R, Roy T, Millam J. GaussView. Version 5. Shawnee Mission (KS): Semichem Inc.; 2009.
26. Frisch MJ, Trucks GW, Schlegel HB, Scuseria GE, Robb MA, Cheeseman JR, et al. Gaussian 09, Revision A.02. Wallingford (CT): Gaussian, Inc.; 2016.
27. Morris GM, Huey R, Lindstrom W, Sanner MF, Belew RK, Goodsell DS, et al. AutoDock4 and AutoDockTools4: Automated docking with selective receptor flexibility. J Comput Chem. 2009;30:2785-91.
28. DeLano WL. The PyMOL molecular graphics system. San Carlos (CA): DeLano Scientific; 2002. Available from: pymol.org (accessed 2020 Nov 12).
29. Molinspiration Cheminformatics. Bratislava (Slovak Republic). 2020. Available from: molinspiration.com (accessed 2020 Nov 12).
30. Sander T, Freyss J, Von Korff M, Rufener C. DataWarrior: An open-source program for chemistry aware data visualization and analysis. J Chem Inf Model. 2015;55:460-73.
31. Lomize MA, Lomize AL, Pogozheva ID, Mosberg HI. OPM: Orientations of proteins in membranes database. Bioinformatics. 2006;22:623-5.
32. Jo S, Kim T, Im W. Automated builder and database of protein/membrane complexes for molecular dynamics simulations. PLoS One. 2007;2:e880.
33. Jo S, Lim JB, Klauda JB, Im W. CHARMM-GUI membrane builder for mixed bilayers and its application to yeast membranes. Biophys J. 2009;97:50-8.
34. Woolf TB, Roux B. Structure, energetics, and dynamics of lipid-protein interactions: A molecular dynamics study of the gramicidin A channel in a DMPC bilayer. Proteins. 1996;24:92-114.
35. Case DA, Cheatham TE III, Darden T, Gohlke H, Luo R, Merz KM Jr, et al. The Amber biomolecular simulation programs. J Comput Chem. 2005;26:1668-88.
36. Skjevik ÅA, Madej BD, Walker RC, Eigen KT. LIPID11: A modular framework for lipid simulations using Amber. J Phys Chem B. 2012;116:11124-36.
37. Wang J, Wolf RM, Caldwell JW, Kollman PA, Case DA. Development and testing of a general amber force field. J Comput Chem. 2004;25:1157-74.
38. Darden TA, York D, Pedersen L. Particle mesh Ewald: An N-log(N) method for Ewald sums in large systems. J Chem Phys. 1993;98:10089-92.
39. Van Gunsteren W, Berendsen H. Algorithms for macromolecular dynamics and constraint dynamics. Mol Phys. 1977;34:1311-27.
40. Lindahl E, Hess B, Van Der Spoel D. GROMACS 3.0: A package for molecular simulation and trajectory analysis. J Mol Model. 2001;7:306-17.
41. Amadei A, Linssen ABM, Berendsen HJC. Essential dynamics of proteins. Proteins. 1993;17:412-25.
42. Berendsen H, Van Der Spoel D, Van Drunen R. GROMACS: A message-passing parallel molecular dynamics implementation. Comput Phys Commun. 1995;91:43-56.
43. Van Der Spoel D, Lindahl E, Hess B, Groenhof G, Mark AE, Berendsen HJC. GROMACS: Fast, flexible, and free. J Comput Chem. 2005;26:1701-18.
44. Gohlke H, Case DA. Converging free energy estimates: MM-PB(GB)SA studies on the protein-protein complex Ras-Raf. J Comput Chem. 2004;25:238-50.
45. Kollman PA, Massova I, Reyes C, Kuhn B, Huo S, Chong L, et al. Calculating structures and free energies of complex molecules: Combining molecular mechanics and continuum models. Acc Chem Res. 2000;33:889-97.
46. Hou T, Wang J, Li Y, Wang W. Assessing the performance of the MM/PBSA and MM/GBSA methods. 1. The accuracy of binding free energy calculations based on molecular dynamics simulations. J Chem Inf Model. 2011;51:69-82.
47. Hou T, Wang J, Li Y, Wang W. Assessing the performance of the molecular mechanics/Poisson Boltzmann surface area and molecular mechanics/generalized Born surface area methods. II. The accuracy of ranking poses generated from docking. J Comput Chem. 2011;32:866-77.
48. Xu L, Sun H, Li Y, Wang J, Hou T. Assessing the performance of MM/PBSA and MM/GBSA methods. 3. The impact of force fields and ligand charge models. J Phys Chem B. 2013;117:8408-21.

49. Sun H, Li Y, Tian S, Xu L, Hou T. Assessing the performance of MM/PBSA and MM/GBSA methods. 4. Accuracies of MM/PBSA and MM/GBSA methodologies evaluated by various simulation protocols using PDBbind data set. Phys Chem Chem Phys. 2014;16:16719-29.
50. Hou T, Li N, Li Y, Wang W. Characterization of domain-peptide interaction interface: Prediction of SH3 domain-mediated protein-protein interaction network in yeast by generic structure-based models. J Proteome Res. 2012;11:2982-95.
51. Sun H, Li Y, Shen M, Tian S, Xu L, Pan P, et al. Assessing the performance of MM/PBSA and MM/GBSA methods. 5. Improved docking performance using high solute dielectric constant MM/GBSA and MM/PBSA rescoring. Phys Chem Chem Phys. 2014;16:22035-45.
52. Liu L, Zhang Y, Wang Y. Phosphine-free palladium acetate catalyzed Suzuki reaction in water. J Org Chem. 2005;70:6122-5.
53. Miyaura N, Yamada K, Suzuki A. A new stereospecific cross-coupling by the palladium-catalyzed reaction of 1-alkenylboranes with 1-alkenyl or 1-alkynyl halides. Tetrahedron Lett. 1979;20:3437-40.
54. Verhulst C, Coiffard C, Coiffard LJ, Rivalland P, De Roeck-Holtzhauer Y. In vitro correlation between two colorimetric assays and the pyruvic acid consumption by fibroblasts cultured to determine the sodium laurylsulfate cytotoxicity. J Pharmacol Toxicol Methods. 1998;39:143-6.
55. Liu Y, Nair MG. An efficient and economical MTT assay for determining the antioxidant activity of plant natural product extracts and pure compounds. J Nat Prod. 2010;73:1193-5.
56. Moreno-Ulloa A, Mendez-Luna D, Beltrán-Partida E, Castillo C, Guevara G, Ramírez-Sánchez I, et al. The effects of (-)-epicatechin on endothelial cells involve the G protein-coupled estrogen receptor (GPER). Pharmacol Res. 2015;100:309-20.
57. Qian H, Xuan J, Liu Y, Shi G. Function of G-protein-coupled estrogen receptor-1 in reproductive system tumors. J Immunol Res. 2016;2016:1-6.
58. Jacenik D, Cygankiewicz AI, Krajewska WM. The G protein-coupled estrogen receptor as a modulator of neoplastic transformation. Mol Cell Endocrinol. 2016;429:10-18.
59. Abe M, Yamashita J, Ogawa M. Medroxyprogesterone acetate inhibits human pancreatic carcinoma cell growth by inducing apoptosis in association with Bcl-2 phosphorylation. Cancer. 2000;88:2000-9.
60. Guo J-M, Xiao B-X, Dai D-J, Liu Q, Ma H-H. Effects of daidzein on estrogen-receptor-positive and negative pancreatic cancer cells in vitro. World J Gastroenterol. 2004;10:860-3.
61. Lonser RR, Glenn GM, Walther M, Chew EY, Libutti SK, Linehan WM, et al. von Hippel-Lindau disease. Lancet. 2003;361:2059-67.
62. Cautain B, De Pedro N, De Escalona MM, Tormo JR, Genilloud O, Vicente F. HCS strategy targeting dysregulation of the VHL/HIF pathway for drug discovery. Adv Biosci Biotechnol. 2013;4:398-405.
63. Rigiracciolo DC, Scarpelli A, Lappano R, Pisano A, Santolla MF, De Marco P, et al. Copper activates HIF-1α/GPER/VEGF signalling in cancer cells. Oncotarget. 2015;6:34158-77.
64. De Francesco EM, Lappano R, Santolla MF, Marsico S, Caruso A, Maggiolini M. HIF-1α/GPER signaling mediates the expression of VEGF induced by hypoxia in breast cancer associated fibroblasts (CAFs). Breast Cancer Res. 2013;15:1-18.
65. De Francesco EM, Pellegrino M, Santolla MF, Lappano R, Ricchio E, Abonante S, et al. GPER mediates activation of HIF1/VEGF signaling by estrogens. Cancer Res. 2014;74:4053-64.